1990 SCA CONFERENCE PAPER NUMBER 9024

NIPER Paper EPR/OP-90/6

PORE LEVEL FLUID IMAGING USING HIGH RESOLUTION NUCLEAR MAGNETIC RESONANCE IMAGING AND THIN SLAB MICROMODELS

by

S. Mahmood, D. Doughty, L. Tomutsa, and M. M. Honarpour

National Institute for Petroleum and Energy Research

For presentation at
Society of Core Analysts

IIT Research Institute
National Institute for Petroleum and Energy Research (NIPER)
P. O. Box 2128
Bartlesville, OK 74005

PORE LEVEL FLUID IMAGING USING HIGH-RESOLUTION NUCLEAR MAGNETIC RESONANCE IMAGING AND THIN SLAB MICROMODELS

by

S. Mahmood, D. Doughty, L. Tomutsa, and M. M. Honarpour
National Institute for Petroleum and Energy Research

ABSTRACT

A fourier transform multinuclear magnetic resonance spectrometer, operating at 270 MHz for protons, was modified into a high-resolution magnetic resonance imaging (MRI) instrument for use in pore level imaging of fluids. The modifications involved the design and construction of a gradient coil assembly to fit over the standard RF probes and development of hardware and software to control the field gradients and for data acquisition. The magnetic field gradients were controlled by using a PC digital-to-analog board. A 3-D projection reconstruction algorithm was adapted to generate 2-D slice images with resolutions down to 25 microns for samples as small as 5 mm diameter. High-resolution MRI was used to study the effect of pore size distribution on fluid flow and trapping in both unconsolidated bead packs and consolidated sandstones. The consolidated samples were selected from outcrop cores containing laminations. The selection was based on flow observation using computed tomography (CT) in the larger cores and optical microscopy in thin slab micromodels (3 mm thick).

In observing flow of fluids through thin-slab rock micromodels, low image contrast hinders the observation of the dynamic behavior of the fluids and of the role of variations in pore geometries on fluid distributions. A new technique which allows improved optical observation of fluid in the rock pore system was developed. Fluid distribution and trapping at pore level were observed by enhancement of low-contrast, low-light images obtained from thin-slab rock micromodels. By combining the high-resolution MRI and optical imaging methods, fluid distributions and dynamics of fluid flow at pore level for both liquid-liquid and liquid-gas displacement processes were studied. These two methods proved to be complementary in defining static and dynamic fluid distribution at pore level. The results indicated that the magnitude and distribution of trapped oil and gas were a function of fluid type and of flow direction in a heterogeneous rock.

INTRODUCTION

Magnetic resonance imaging (MRI) has developed into a versatile tool for non-invasive investigations of tissue structure in clinical and biological fields because of its unique capability to detect and spatially display various fluid and tissue components and their distribution within plant and animal tissues. In the past several years, this capability of MRI has been applied in investigations of fluids in porous rock, showing how fluid distribution and properties are related to rock structure (Rothwell and Vinegar, 1985; Baldwin and Yamanashi, 1986; Blackband, et al., 1986; Hall, et al., 1986; Doughty and Maerefat, 1988; Edelstein, et al., 1988; Doughty and Maerefat, 1989). Many of these MRI studies have involved instruments developed for clinical work which have a spatial resolution limit of about 0.5 mm. This resolution is adequate for displaying the gross fluid distribution in rock along with the effects of larger-scale rock structures such as layering, but the physics of the rock-fluid interaction occurs at the pore level and is determined by the effects of pore shape, size, and connectivity on a three-dimensional basis along with the nature of the pore surface and fluid properties. The recent development of MRI microscopy, in which a magnetic field gradient coil system having superior gradient strength and switching characteristics is added to a standard high-resolution nuclear magnetic resonance (NMR) spectrometer, has resulted in improved MRI resolutions as high as 10 microns for plant and animal tissues (Kuhn, 1990). At these resolutions, which are lower than typical pore sizes, the actual distribution of fluids within a pore can be studied as a function of system parameters. Unfortunately, the characteristics of rock/fluid interactions at higher NMR frequencies with resulting short spin-spin relaxation times and broader NMR signals prevent many of the techniques developed for biologic MRI microscopy from working in studies of rock/fluid systems (Kuhn, 1990). We have attempted to exploit some of these developments in MRI microscopy by constructing a gradient coil system to fit over standard NMR sample probes. This system uses the multinuclear capability of the NMR spectrometer to image both proton- and deuterium-containing fluids to operate two-phase MRI of fluids in porous rock. The technique of projection reconstruction has been expanded to three-dimensions permitting the complete imaging of a sample volume to a resolution as high as 25 microns for fluids in polymer bead packs. The methodology has also been used to image two-phase fluid distribution in Berea and Shannon sandstone samples at lower resolutions of 120 microns.

Micromodels of various types have been used to model rock-fluid interactions and permit the observation of interactions otherwise concealed by the rock matrix. Conventional micromodels belong to one of three classes: capillary tubes, unconsolidated or artificially consolidated bead packs, or pore network models. Capillary tube models, due to their simplicity, are ideal for mathematical modeling, but may not represent microscopic behavior in reservoir rocks. Artificial bead pack models suffer from fluid by-passing between the beads and glass plates which almost always overwhelms the expected behavior. Bead packs also suffer from bead migration during flow experiments . Artificially consolidated bead packs, such as cryolite models, can reduce the effect of these problems, but the original pore configuration is

usually significantly altered. Bead packs do offer a more realistic pore geometry compared to capillary tubes but are deficient in representing the heterogeneous nature of rock's wetting characteristics and pore/throat geometry. Pore network models are a compromise between the above two models and are free from many problems such as fluid by-passing and grain migration. Limitations for pore network models are their strict two-dimensionality and their departure from realistic pore/throat configurations. The new technique of rock-slab micromodels recently developed allows direct observation of fluids in rock at the pore level (Mahmood and Maerefat, 1988). Such a direct visual observation was found to be useful in understanding 2- and 3-phase flow and fluid entrapment. The advantage over conventional models is the capability for observing fluid behavior in original reservoir rocks rather than overly simplified pore/grain systems. Because of pore-level geometric similarity, the observations are somewhat more realistic than those of simplified models: flow is three-dimensional on a microscopic scale, and fluid by-passing through the boundary is completely eliminated. Comparison of rock-slab models with conventional models has been reported (Mahmood, 1990). In that work, drainage and imbibition tests were performed in three types of micromodels: heterogeneously etched glass network, artificially consolidated cryolite, and rock-slab. This work involved tests in layered Berea and glauconite-laminated Shannon sandstones.

This joint approach of using rock-slab micromodels and MRI microscopy to investigate rock/fluid interactions at the pore level utilized the complementary nature of the two techniques. The results of this research show that optical microscopy used with rock-slab micromodels offers excellent resolution and also permits dynamic imaging of slow/medium flow systems and the investigation of rock/fluid interactions. MRI is selective in imaging only one of the phases at a time and can image the fluids in a larger scale sample while eliminating any interference from the rock matrix thus offering true three-dimensional investigations at the macroscopic level.

ROCK CHARACTERIZATION

(A) Petrographic analysis of Berea and Shannon Sandstones

The macroscopic examination of the Berea rock revealed a porous sandstone with only subtle layering seen in reflected light. The pores were discontinuous in the poorly defined "higher" porosity zones. The microscopic examination of the rock composition based on visual scan of the thin section includes: quartz 56%, feldspars 2%, rock fragments 10%, clay cement 3%, calcite cement 2%, heavy minerals 1%, and muscovite <1%. Diagenetic clays are not concentrated into beds or layers in this sample, but are instead approximately evenly distributed. Layering is not apparent within the thin section using the petrographic microscope. All that can be recognized are slightly more porous or slightly less porous areas that tend to be elongate. Such areas cannot be traced in bands visually along the known

bedding direction and they are discontinuous. Layering of porosity in this sample may be determined statistically.

One potential method for determining more or less porous zones is to count the number of contacts a given grain has with adjacent framework grains. In this sample, there is a significant difference between the number of grain contacts in more porous areas (average 3.5 contacts per grain) compared with the less porous areas (average 5.4 contacts per grain). These results tend to reflect differences in packing of grains within the sandstone. The "contact index" could be mapped to determine lineation or trend (porous vs. more grain-dense layers) in samples in which layering may not be visually apparent.

The macroscopic examination of the Shannon rock revealed a porous sandstone with cross laminations readily apparent in transmitted or reflected light. Cross laminae are visually enhanced by brown coloration which contrasts with the blue-dyed epoxy of the more highly porous layers. The microscopic examination of the rock composition based on visual scan of the thin section includes: quartz 22%, chert 4%, feldspars 15%, rock fragments 2%, glauconite 25%, clay cement 1%, and micas 1%. The most characteristic feature of this rock sample is the abundance of rounded to compacted glauconite grains, which are the source of the brown to greenish brown coloration of some layers. Layering in this sample is created by the contrast of highly compacted glauconitic laminae with less compacted, less glauconitic, more porous laminae. Glauconite grains are soft and easily compacted between more rigid framework grains such as quartz, chert, or feldspar. The contact index (number of grain contacts) within compacted, glaucinite-rich laminae averages 5.8 but only 4.0 in the more porous, glauconite-poor laminae. Another difference between the two types of laminae is that the pores are much larger (average 100-150 microns diameter) in the more porous laminae than in the compacted laminae (average 50 to 70 microns diameter). In addition, the compacted laminae have a significantly larger proportion of completely collapsed pores.

The Shannon sample in contrast to the Berea sandstone sample has layering that is more visually apparent. "Grain dense" layers were created by compaction, particularly of glauconite, and the compacted laminae are more laterally continuous. In addition, the mineralogical composition and rock types represented by the two samples are quite different.

(B) Petrophysical properties and CT Scans of Berea and Shannon sandstones

Figure 1 shows the variation in CT densities for the layered Berea and Shannon sandstones. The variation in CT density due to change in porosity is significant. Table 1 shows the range of porosity and permeability values obtained from computerized petrographic image analysis (PIA) of these sandstones. The average values obtained for both porosity and permeability of the Berea sandstone using PIA agree

well with the values obtained from routine core analysis. The average value for porosity for the Shannon sandstone using PIA agrees very well with that from routine core analysis but the permeability values are quite different.

Table 1. - Porosity and permeability comparison of petrographic image analysis and core analysis of Berea and Shannon sandstones

	Berea		Shannon	
	PIA[1]	Core analysis	PIA[1]	Core analysis
		Porosity, %		
Highest value	31.0	—	44.0	—
Lowest value	10.0	—	18.0	—
Average value	19.0	18.7	30.0	30.4
		Permeability, mD		
Highest value	2,170	—	11,906	—
Lowest value	8	—	141	—
Average value	294	300	2,253	930

[1]Petrographic image analysis.

EXPERIMENTAL EQUIPMENT AND MICROMODEL FABRICATION TECHNIQUES

The experimental setup consisted of a modified geological microscope, a powerful fiber optic light source, a sensitive high-resolution monochromatic video camera (Plumbicon tube, 0.005 lux, 900 TV-lines), and a super-VHS VCR (450 lines). For photography, an automatic 35-mm camera was attached.

Figure 2 shows assembly details of a rock-slab model. It essentially consisted of an actual rock slab of 2 to 3 mm thickness sandwiched between two plexiglass plates. Gaskets were used to confine the flow to the rock; in addition a coating of soft and transparent silicone rubber was applied to eliminate by-passing through the adjoining rock/plexiglass surfaces. A description of the model has been reported (Mahmood and Maerefat, 1988). For the flow experiments the three phases used were 1% NaCl brine, Soltrol (5cp) mineral oil with red dye, and nitrogen gas from a cylinder. A description of the experiments and details have been reported previously (Mahmood, 1990).

One of the important advantages of rock-slab models over packed models is that fluid by-passing through adjoining boundaries between grains and encapsulating plates can be completely eliminated. By-passing, which is very common in most packed micromodels, can completely distort the flow behavior. The top-layer of grains in a rock-slab model imbeds in transparent silicon-rubber coating, making a strong bond. The grains in a sandpack, on the other hand, are not consolidated and contain enough clearance to re-adjust when exposed to pressure, thus, allowing the by-passing.

The highest quality of observations and reproductions is possible for slow events spanning over 10's of minutes, such as foam degradation, emulsification, and interactions at rock/fluid interfaces. The faster the events under observation, the lower the quality of reproductions because of the low-light views requiring several minutes exposure time with an ASA 125 film. In this work quality was poor but acceptable for dynamic events occuring at moderate speeds (10 to 20 ft/day). Difficulties were observed when mass-reproducing events faster than this speed, such as foam formation, foam rupture, and most capillary-controlled phenomena occurred. The quality of video recordings of these events was also marginal. For extremely difficult situations, direct observations through the microscope were used.

MRI EXPERIMENTAL TECHNIQUES

A shielded magnetic gradient coil system was designed and built to fit over the standard high-resolution NMR sample probes for a JEOL GX-270 NMR spectrometer. This spectrometer operates at a frequency of 270.16 MHz for protons and 41.47 MHz for deuterium at a field strength of 6.34 Tesla. The gradient system is capable of generating gradients in the X, Y, and Z directions of 350 mT/m. The gradient strength and direction are controlled by signals from three digital-to-analog converters (DAC) on a Real Time Devices (RTD) model DA600 12-bit D/A board driven by a PC/XT. The gradients are turned on and off by a trigger from the spectrometer pulse programmer to a RTD model DG96 digital I/O board in the PC. A program in the PC monitors the I/O board for the trigger, updates the gradient signals for each coil, and outputs the gradient signals for the specified time period. The number of gradient steps in the imaging sequence to achieve the desired resolution are input as parameters at the start of the program. The gradient signals to each coil are amplified by three Techron 7520 amplifiers (DC to 20,000 Hz).

To image a sample in three dimensions by the projection reconstruction technique, a gradient of constant magnitude must be swept through all possible directions in a hemi-spherical space. This involves sending the appropriate components to each of the three orthogonal gradient coils in sequence to sweep the gradient through the desired pattern. At each position of the gradient, an NMR signal is acquired which, when fourier transformed, represents the profile of the proton or deuteron distribution across the sample along the direction of the gradient. A computer program reads these proton or

deuteron projections in sequence and reconstructs the spatial distribution of the nuclei within the sample volume and forms the image as a display of pixel intensity (nuclei concentration) as a function of position across the sample.

The data are transformed in the spectrometer data-acquisition computer and then sent to a Gateway 2000 33-MHz 386 computer with a Weitek 3167 numeric coprocessor. The data file for a 3-D MRI image having a resolution of 128 pixels in each direction occupies 8 megabytes. Processing this data file and reconstructing the image requires slightly less than 1 hour on the 386 computer, and the output can be displayed as a stack of X/Y, X/Z, or Y/Z "slices" of the sample. If lower resolution is desired, shorter computation time is involved. Conversely, if higher pixel resolution is desired, much longer time is involved and much larger data files are involved.

Samples of various types are contained in all-Teflon sample holders supported in 10-mm glass tubes to avoid proton signals from the holders. For sand or polymer bead packs, 1/4-inch-diameter Teflon tubing having an ID of 4.7 mm was fitted with Teflon end caps containing 1/16-inch small-bore Teflon tubing. The beads or sand was packed inside the tubing section providing a sample about 8 mm long and 4.7 mm diameter. For the Berea and Shannon sandstone samples, small cylindrical plugs 5 to 6 mm diameter and 8 mm long were cut from bulk rock samples. Both rock plugs were selected to contain at least one visible lamination running along the axis of the cylinder. The Berea plug had one lamination and the Shannon plug had two. The Shannon rock was very friable, so the resulting shape of the plug was somewhat irregular. Teflon end caps with 1/16-inch tubing were made, and the rock plug and caps were placed inside Teflon shrink tubing: heating the shrink tubing formed a fairly tight-fitting container for the rock plugs. The samples in their holders were evacuated and saturated with 1% NaCl in 99.6% deuterium oxide (heavy water) as the aqueous phase. A deuterium MRI image of each sample was obtained: the resolution for the bead packs was 128x128x128, and that for the rock samples was 64x64x64. For the deuterium images of the packs, four signals at each gradient position were added to improve signal/noise ratio, while for the rock plugs eight signals were added. A 25-degree RF pulse was used with a 0.25-second interpulse delay.

For the two-phase MRI experiments, Soltrol mineral oil (5-cP viscosity) was used as the oil phase. Red dye was used to color the oil phase to track its progress visually. For the packs, a syringe was used to push about 5 pore volumes of oil through the pack in about 10 minutes. The rock plugs were immersed vertically in the oil phase and centrifuged at 1,500 rpm for 4 hours to allow the oil phase to displace the aqueous phase. A proton MRI image was obtained for each sample to see the oil phase, and a second deuterium image was obtained without moving the sample to see the residual aqueous phase. The same respective resolutions were used as above for each sample. For the proton image, 2 signals were added at each gradient position with a 0.5-second interpulse delay and a 25-degree RF pulse. (The oil had a

longer spin-lattice relaxation time than the deuterium oxide.) Because the residual deuterium oxide was much less concentrated, 8 or 16 signals were added, respectively, for the packs or rock plugs to improve signal/noise ratios. After processing the data for the two-phase systems, a computer program was written to display the data in a color image with the deuterium (aqueous) image displayed as levels of cyan and the proton (oil) image as levels of yellow to simultaneously show the complementary distribution of the two phases. Single-phase images were displayed as gray-scale images.

RESULTS AND DISCUSSION FROM MICROMODEL STUDIES

For various non-limiting reasons, the flow tests in rock-slab micromodels have so far been exploratory. Only one color-Xerox plate (Figure 3) containing seven photographs is included in this paper. In the Figure the oil phase is orange, the brine phase is green or blue and the gas phase appears as bubbles. The figures have been selected to serve as examples for the type of observations obtained at magnifications ranging from 4X to 500X (in descending order from A to G). A noticeable loss in quality (decreasing the depth of view) has occurred in Xeroxing. Photomicrographs at still higher magnifications are also possible. An example photomicrograph at 1200X magnification is shown in black and white in Figure 4. Such higher magnifications are desirable for observing rock/fluid interactions, microemulsions, and microbial interactions.

Figure 3 (A) shows two oil blobs in a pore (500X) of the Shannon rock remaining after secondary imbibition, i.e. after the following cycle: initial brine injection in dry rock/oil injection until brine production stops/brine reinjection until oil production is stopped. However, most of the oil remaining at residual oil conditions did not have this configuration. Instead, most of the pores containing oil were almost completely filled with it, except in crevices and thin coatings of brine on the grain surfaces [Figure 3 (B), Shannon rock, 260X]. Another common observation was the trapping of oil ganglia extending over several pores due to the viscous by-passing of displacing brine [Figure 3 (E), Berea rock]. Figure 3 (C) is a photograph of the central region of Figure 3 (E) showing this behavior at four times higher magnification.

Figure 3 (D) shows the distribution of all three phases, (oil, gas, and brine) in Shannon rock during gas injection into the oil- and brine-filled micromodel. Gas propagated in the form of small isolated bubbles through oil-filled channels, thus producing oil. After the moveable oil was produced, gas then displaced brine.

Figure 3 (G) shows the fingering during oil (5-cP) injection into a brine-filled homogeneous Berea rock-slab model at 4X. Fingering was not evident in the layered Shannon rock-slab model because the heterogeneities diffused the fingers. Oil front advancement was rather layer-after-layer type, i.e., the layer closest to the injection port was swept first, then the second layer, and so on. The tighter the layers were,

the more the brine was held in them. Brine saturation was also higher near the producing end due to the end effects. This stratified nature of fluid distribution is shown in Figure 3 (F) at 10X magnification.

Use of a 2 to 3 mm rock slab introduces certain complexities in the observations. The flow is neither strictly two-dimensional as in network models, nor is it truly three-dimensional on a macro-scale. Also, the pore-to-pore connection is lost for some pores adjoining the encapsulating (no-flow) boundaries. These factors limited the ability to visualize the entire network of pores, and fluid flow and trapping through selected pores which are strategically located were monitored. These limitations are not expected to significantly alter the flow mechanism. For example, consider a hollow sphere in which the flow in and out is through 10 symmetrically located small tubes. If this system is cut in half and enclosed with a flat plate at the cutting plane, the basic flow mechanism is not expected to change drastically, if at all. Besides, there are some locations where an inner pore can be viewed, either through microfractures/cavities, or in situations where a group of grains are vertically aligned.

The effect of dissimilarity in the wettabilities of the transparent silicon-rubber coating (preferentially oil-wet) and the rock grains could be important. The oil-wetting on the confining boundary was manifested only after 10s of hours, which was enough duration to complete a test. On gas injection, however, the water films between oil and silicon-rubber surfaces were broken, gradually causing an oil-wetting problem. Once it happened, the model had to be discarded because the process was irreversible..

The most serious concern one should have about any micromodel is the effect of neglecting scaling criteria. Satisfying them simultaneously for both macro- and microscopic levels is more difficult in micromodels than in core plugs, because of the smaller overall dimensions of the core. For example, if residual wetting phase saturation was 25% in a core plug, it would be much less in a micromodel made from a rock slab from the same core plug. In rock plugs, there are regions unswept due to viscous by-passing. Because of smaller size, this by-passing is not identical in rock-slab micromodels. Further studies are needed to understand the true extent of this limitation.

The optical microscopy used with rock-slab micromodels offers very good resolution down to micron level and also permits dynamic imaging of slow/medium flow systems and the investigation of rock/fluid interactions. However, the pore structure is modified by the limitation to 2 to 3 mm-thick slabs for adequate light transmission and the presence of the confining windows which add boundary/wettability variation problems.

RESULTS AND DISCUSSION, FROM MRI IMAGING STUDIES

Figure 5 shows the results for the Shannon sandstone plug (a, b), the Berea sandstone plug (c, d), and the polymer bead pack (e, f). Shown for each sample is an X/Y-section and a vertical section. The oil phase is displayed in yellow and the aqueous phase in cyan. The green color indicates areas where both phases are present in the same pore space. For the rock images, the brighter yellow to yellow-white areas at the ends or around the perimeter of the images are regions where bulk oil was trapped between the sample holder and the plug. The pixel resolution for the rock plugs was 120 microns, and that for the polymer bead pack was 50 microns.

The X/Y-section of the Shannon plug (figure 5(a)) shows the two laminations as regions of lower fluid content, one in the lower left and the other in the upper right of the image. These laminations were not as visible in the initial one-phase water image, so centrifugation seems to have selectively depleted the fluids in the darker bands indicating possibly better flow characteristics for these zones. This section is in the lower half of the plug about two-thirds down from the top of the plug. The vertical section (figure 5(b)) for the Shannon plug is an X/Z view through the center of the plug. The laminations visible in (a) appear here as the darker vertical bands on the left and right sides of the image. The oil phase is more prominent in the upper part of the image and also at reduced saturation in the laminations.

The X/Y-section of the Berea plug (figure 5(c)) is from the upper half of the plug about one-fourth down from the top. The lamination is visible as the more blue band running through the center of the image from lower right to upper left. Compared to the Shannon images, the Berea appears to have less fluid content, consistent with its lower porosity, and a much more heterogeneous appearance. The vertical section (figure 5(d)) is a Y/Z view through the center of the plug. The water displacement by the oil phase in this plug appears to have a distinct front just below the center of the plug with predominantly oil above and water in the lower part of the plug though there are a few areas where pockets of water were apparently left behind in the upper half of the plug. The lamination is somewhat evident in the center of the vertical image particularly in the upper half.

The two images of the bead pack (figure 5(e), (f)) are much sharper from the higher resolution obtained. In this pack, the beads were spherical and had a size range from 350 to 500 microns. The circular profile of individual beads is evident in the two images. The vertical section (figure 5(e)) is an X/Z section through the center of the pack. The oil phase is predominant in the upper half of the image with the water phase in the lower half. There are pore spaces where the aqueous phase was bypassed during the displacement, leaving pockets of water in individual pore spaces. Also, the oil phase apparently displaced water preferentially in the outer perimeter of the pack leaving higher water content in the center of the pack nearer the bottom. The X/Y section (figure 5(f)) is a view near the bottom of the pack showing

the higher water content in this region. However, the water displacement was not uniform with a region of oil evident in the right half of the image. The larger irregular dark areas evident in both images probably indicate the presence of gas bubbles trapped in some of the pore spaces.

The decision to display the rock images at a lower resolution than that of the bead pack was based on the respective properties of the NMR signals from the two types of samples. The fluids in the rock matrix had a natural NMR line width of 700 Hz for deuterium and 2,000 Hz for protons. The gradients available were able to spread this signal to approximately 14,000 Hz and 40,000 Hz, respectively, for the 5-mm diameter of the samples. Thus the physical resolution obtainable was about 200 to 250 microns for the rock images (Kuhn, 1990). This natural line-width is affected by the chemical composition of the sample, particularly the presence of paramagnetic and ferromagnetic nuclei such as copper, manganese, or iron contained in clays. To acheive meaningful higher resolution will require stronger gradients to spread the signal more or selecting rock with lower contents of the paramagnetic nuclei. For the polymer bead pack the NMR line widths were 20 and 120 Hz, respectively, indicating that the higher displayed resolution was meaningful. Additional development could permit the attainment of resolutions with MRI of rock/fluid systems of 20 microns.

The NMR sample probes for the spectrometer used in this work have the multinuclear RF coil located inside the proton RF coil. The materials used to fasten the RF coil in place contain protons and give a broad signal which does not affect high-resolution NMR spectroscopy but creates some interference for the broad signals obtained in MRI in the presence of the gradients. This factor caused the appearance of artifacts in the proton images of the rock samples where the fluid saturations were low. To eliminate this problem will require the construction of a sample probe with the proton coil inside the deuterium coil and/or the elimination of any materials containing protons for the inner coil.

This approach to MRI microscopy using 3-D projection reconstruction is computer-intensive because of the large data files involved. Also, the experiments are time-consuming, particularly with the deuterium images of residual water where several signals must be added to get adequate signal/noise ratios. Therefore, the experiments necessarily must be static in nature. To go much beyond 128-pixel resolution probably would require a parallel processor computer system having several processors to speed computions and display. One advantage of the projection reconstruction approach is the built-in parallel nature of the data processing permitting an easy transition.

MRI microscopy is unlikely to ever approach the resolution of optical microscopy and is unlikely to obtain the speed of image acquisition which would permit dynamic experiments. However, MRI is selective in imaging only one of the phases at a time thus eliminating a possible source of confusion in the interpretation of multiple phase systems. Also, MRI can see the fluids in a larger scale sample while

eliminating any interference from the rock matrix thus offering true three-dimensional, pore system, fluid distribution investigations at the macroscopic level.

CONCLUSIONS

1. MRI microscopy and rock-slab micromodels are two powerful techniques useful for pore-scale fluid-flow investigations.

2. The complementary nature of the techniques of rock-slab micromodels and MRI microscopy permits the comprehensive investigation of rock/fluid interactions and fluid flow characteristics in porous rock down to the pore level.

3. Even small laminations in heterogeneous porous rock have important effects on initial fluid distribution, fluid flow, and hydrocarbon trapping.

ACKNOWLEDGEMENTS

This work was supported in part by the Department of Energy under cooperative agreement DE-FC22-83FE60149. The help of Rick Schatzinger for petrographic analysis and Alan Brinkmeyer for CT work is gratefully acknowledged. The assistance of Tom Burchfield, Min Tham, Mike Madden, and Bill Linville is also appreciated.

REFERENCES

Rothwell, W. P. and Vinegar, H. J. (1985) "Petrophysical Applications of NMR Imaging," *Applied Optics*, v. 24, p. 3969.

Baldwin, B. A. and Yamanashi, W. X. (1986) "Detecting Fluid Movement and Isolation in Reservoir Cores Using Medical NMR Imaging Techniques," Presented at the Fifth SPE/DOE Symposium on Enhanced Oil Recovery, Tulsa, Oklahoma, Apr. 20-23, SPE/DOE Paper 14884.

Blackband, S. P., Mansfield, P., Barnes, J. R., Claque, A. D. H., and Rice, S. A. (1986) "Descrimination of Crude Oil and Water in Sand and Berea Cores with NMR Imaging," *SPE Formation Evaluation*, Feb., pp. 31-34.

Hall, L. D., Rajanayagam, V., and Hall, C. (1986) "Chemical-Shift Imaging of Water and n-Dodecane in Sedimentary Rocks," *J.Magn. Reson.*, v. 68, p. 185.

Doughty, D. A. and Maerefat, N. L. (1988) "Modification to a JEOL GX270 Widebore Spectrometer for Magnetic Resonance Imaging: Petrographic Applications," Poster Session, 29th Experimental Nuclear Magnetic Resonance Spectroscopy Conference, Rochester, N Y, Apr.17-21.

Edelstein, W. A., Vinegar, H. J., Tutunjian, P. N., Roemer, P. B., and Mueller, O. M. (1988) "NMR Imaging for Core Analysis," Presented at the 63rd Annual Technical Conference and Exhibition of the Society of Petroleum Engineers, Houston, TX, Oct. 2-5, SPE paper 18272.

Mahmood, S., and Maerefat, N. L. (1988). "New Techniques of Pore-Scale Visualization of Fluids in Porous Media: The Effect of Pore Structure on Fluid Distribution." Department of Energy Report. No. NIPER-372, Sept.. NTIS Order No. DE89000731.

Doughty, D. A. and Maerefat, N. L. (1989),"Preliminary Transformation of an NMR Spectrometer into an NMR Imager for Evaluating Fluid Content and Rock Properties of Core Samples.", *Log Analyst*, Mar.-Apr., pp. 78-83.

Kuhn, W., (1990), "NMR Microscopy - Fundamentals, Limits, and Possible Applications.", *Angew. Chem. Int. Ed. Engl.*, v. 29, Jan., pp. 1-19.

Mahmood, S. M. (1990) "Fluid Flow Behavior Through Rock-Slab Micromodels in Relation to Other Micromodels," Department of Energy Report. No. NIPER-448, Sept. NTIS Order No. DE90000244.

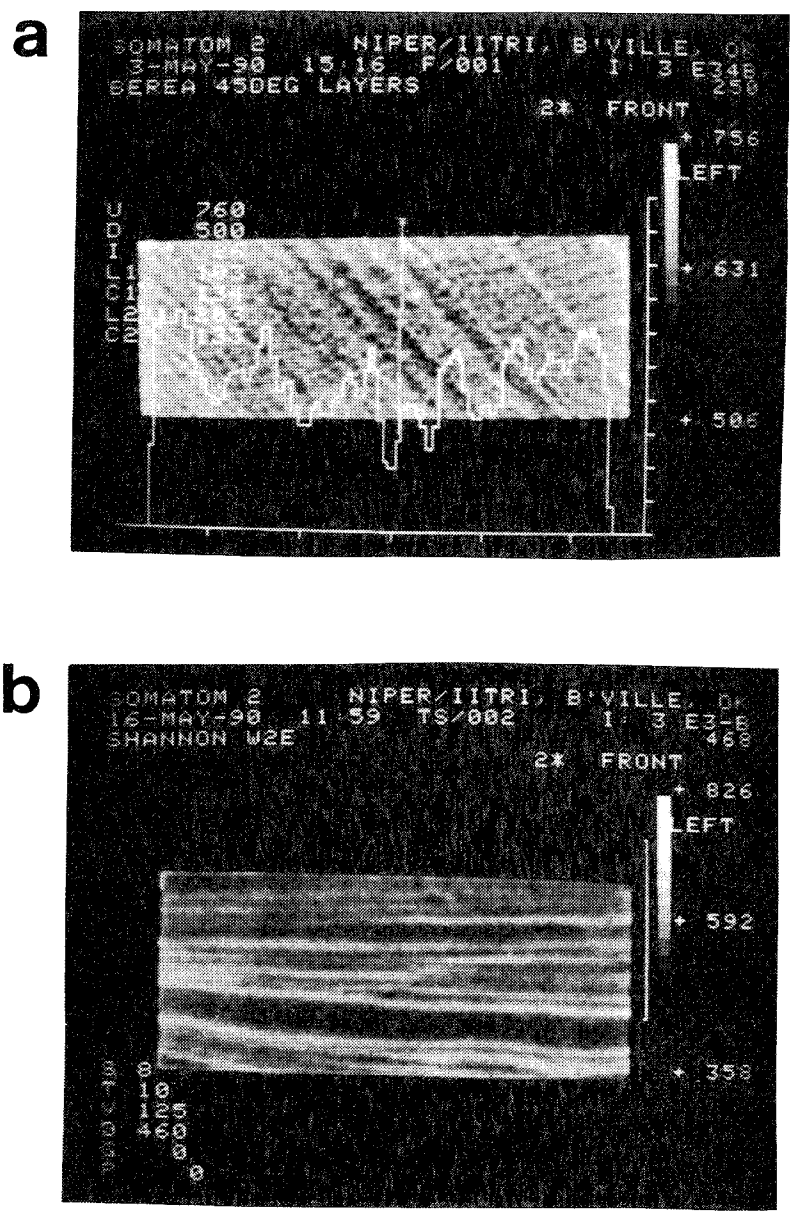

Figure 1, (a, b). CT images of Berea and Shannon sandstones showing variations in CT density. (a) Berea sandstone (upper). (b) Shannon sandstone (lower).

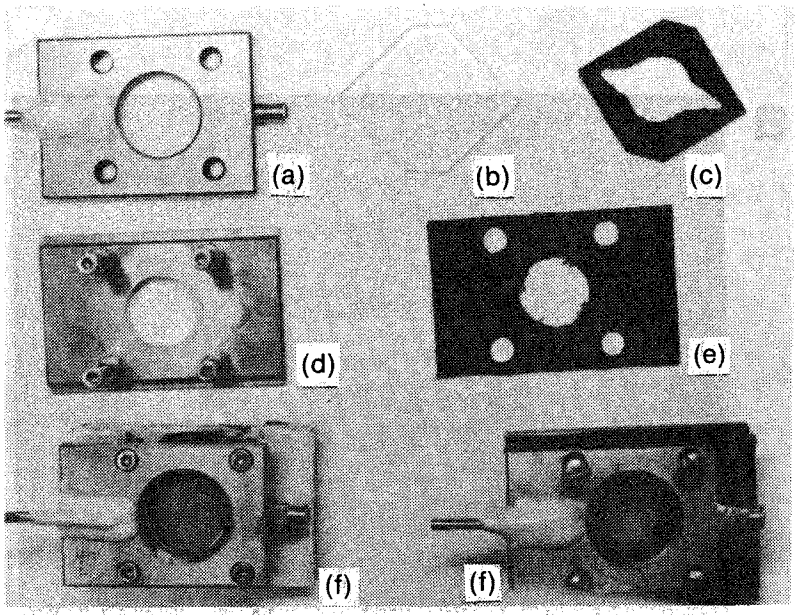

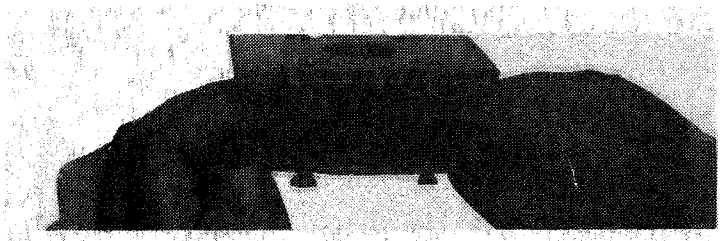

(g)

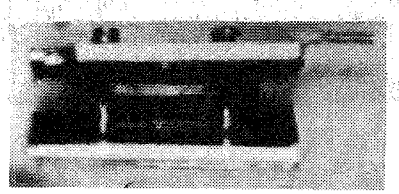

(h)

1 cm.

Figure 2. Details of rock-slab micromodel: (a) upper metal frame, (b) plexiglass plate coated with clear silicone rubber, (c) central rubber gasket to house the rock slab, (d) lower metal frame, (e) rubber gasket seal between a and b, (f) completely assembled model, (g) and (h) are partially assembled to show details.

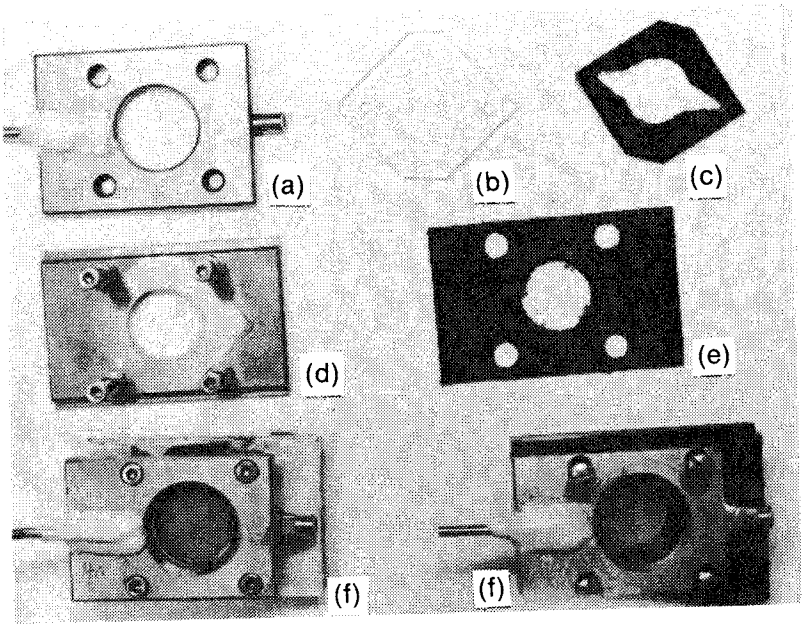

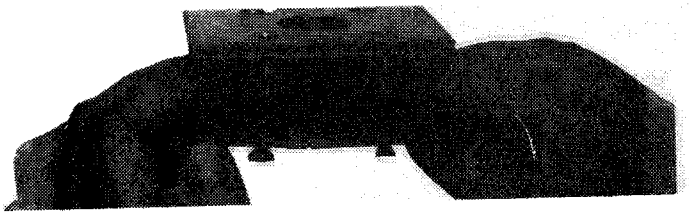

(g)

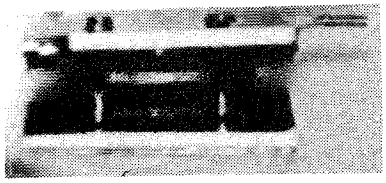

(h)

1 cm.

Figure 2. Details of rock-slab micromodel: (a) upper metal frame, (b) plexiglass plate coated with clear silicone rubber, (c) central rubber gasket to house the rock slab, (d) lower metal frame, (e) rubber gasket seal between a and b, (f) completely assembled model, (g) and (h) are partially assembled to show details.

Figure 3, (A-G). Color photomicrographs of Berea and Shannon sandstone rock-slab micromodels. Orange shows the oil phase and green shows the brine and brine-coated rock grains. Bubbles are the gas phase. (A) Shannon sandstone after secondary imbibition at 500X magnification. (B) Shannon sandstone at 260X magnification. (C) Berea sandstone showing oil ganglia. (D) Shannon sandstone with three phases (oil, gas, and brine. (E) Berea sandstone at lower magnification. (F) Berea sandstone showing stratified fluid distribution of oil and brine at 10X. (G) Berea sandstone showing fingering of oil into brine at 4X.


A

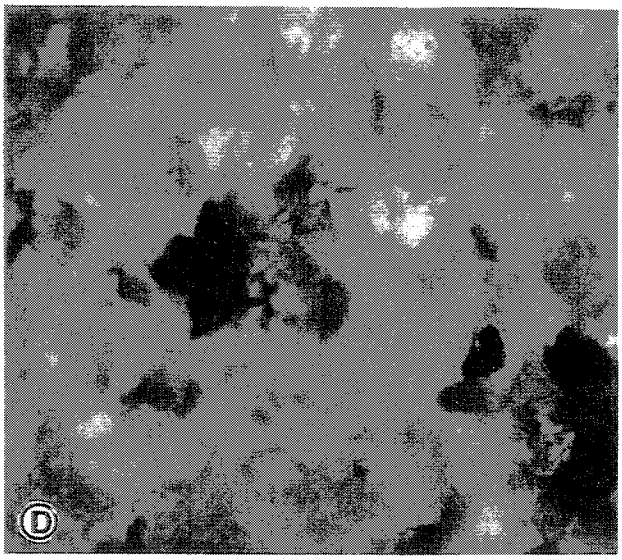
D

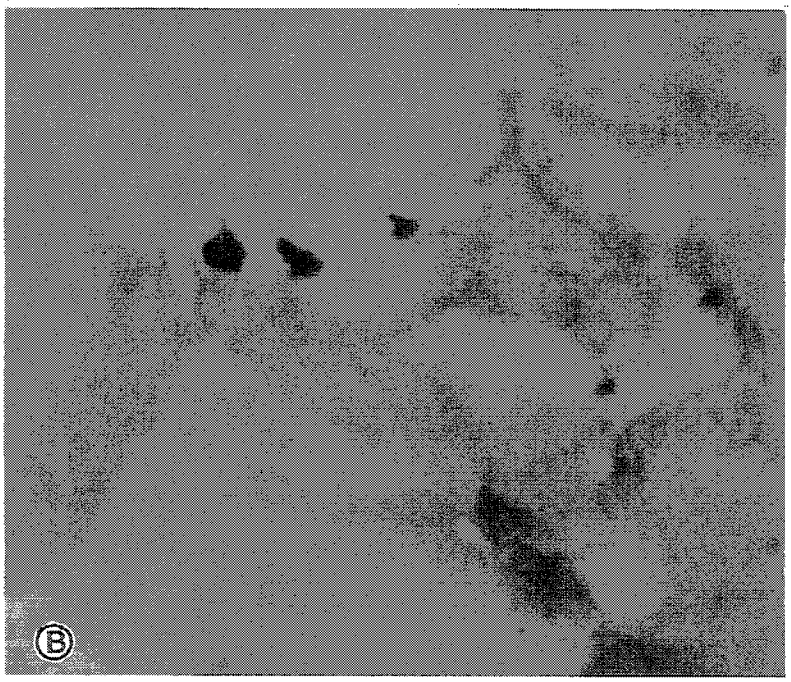
B

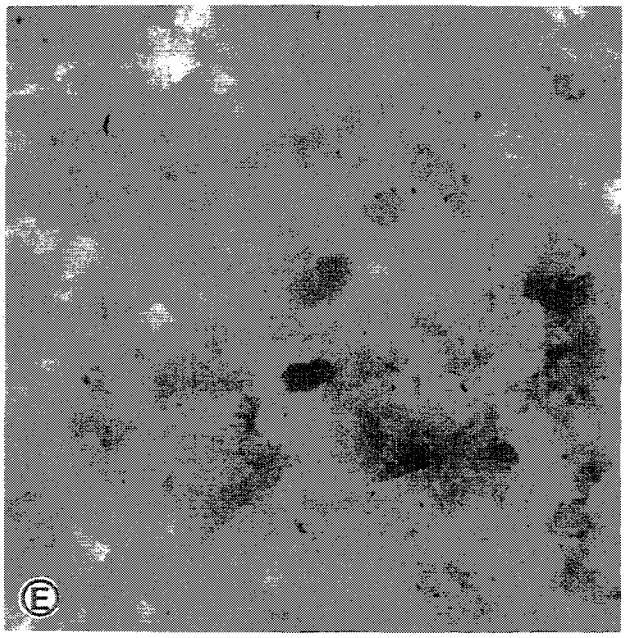
E

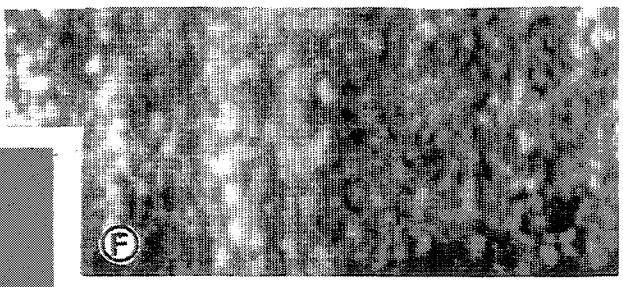
F

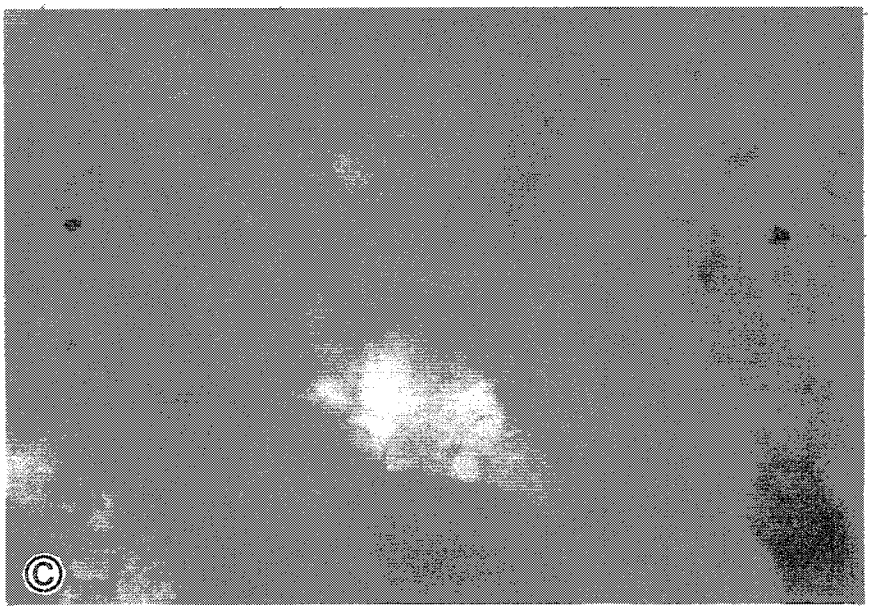
C

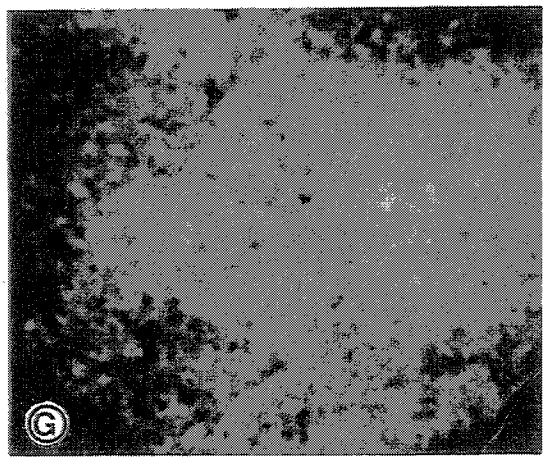
G

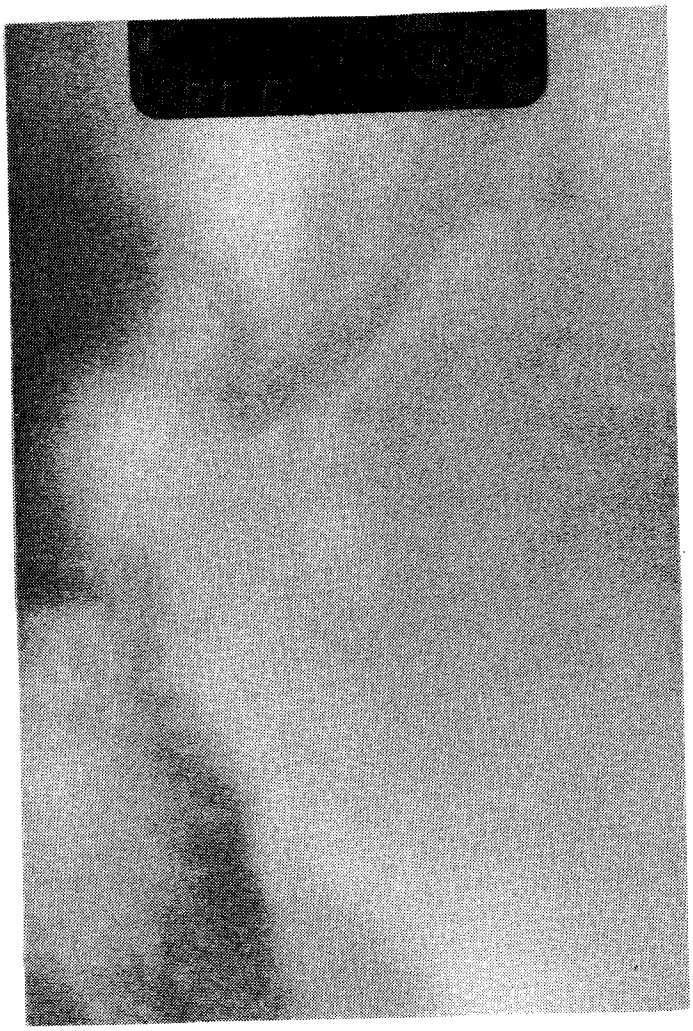

Figure 4. High magnification (1200X) photomicrograph of rock-slab micromodel.

Figure 5, (a-f) MRI images of two-phase fluid distribution in sandstones and bead packs. The oil phase is shown in yellow and the aqueous phase is shown in cyan. The pixel resolution for the sandstone plugs is 64x64 and that for the bead pack is 128x128. (a) X/Y-section of Shannon sandstone plug 6 mm dia. and 7 mm long. (b) X/Z-section of Shannon plug. (c) X/Y-section of Berea sandstone plug 5 mm dia. and 8 mm long. (d) Y/Z-section of Berea plug. (e) X/Z-section of polymer bead pack 4.7 mm dia. and 9 mm long. (f) X/Y-section of polymer bead pack.o

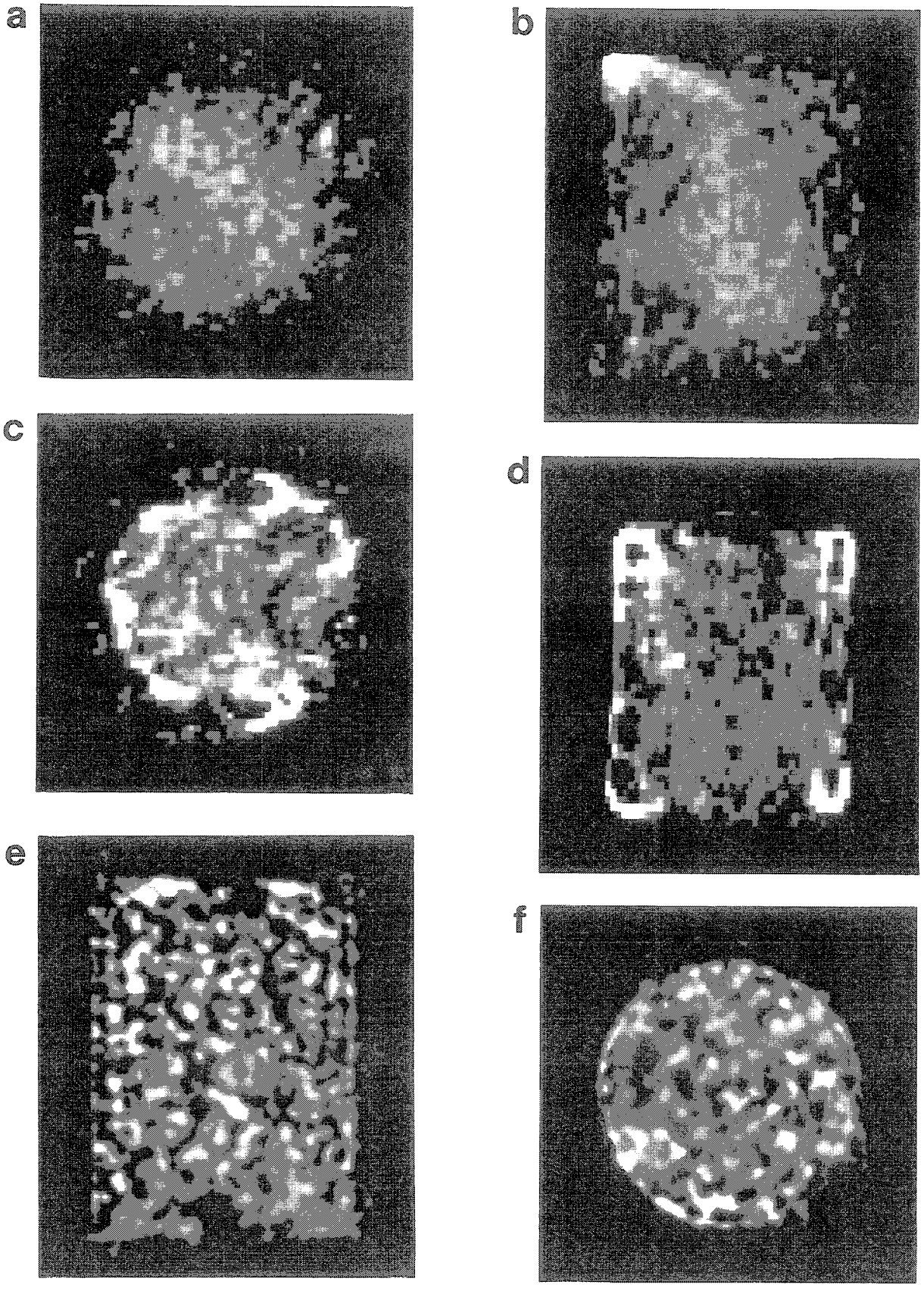
a
b
c
d
e
f